

# Full density matrix dynamics for large quantum systems: Interactions, Decoherence and Inelastic effects

Manas Kulkarni and Kunal L. Tiwari

*Chemical Physics Theory Group, Department of Chemistry, University of Toronto,  
80 Saint George St. Toronto, Ontario, Canada M5S 3H6 and  
Department of Physics, University of Toronto,  
60 Saint George St. Toronto, Ontario, Canada M5S 1A7*

Dvira Segal

*Chemical Physics Theory Group, Department of Chemistry,  
University of Toronto, 80 Saint George St. Toronto, Ontario, Canada M5S 3H6*

(Dated: September 11, 2021)

## Abstract

We develop analytical tools and numerical methods for time evolving the *total* density matrix of the finite-size Anderson model. The model is composed of two finite metal grains, each prepared in canonical states of differing chemical potential and connected through a single electronic level (quantum dot or impurity). Coulomb interactions are either excluded all together, or allowed on the dot only. We extend this basic model to emulate decohering and inelastic scattering processes for the dot electrons with the probe technique. Three methods, originally developed to treat impurity dynamics, are augmented to yield global system dynamics: the quantum Langevin equation method, the well known fermionic trace formula, and an iterative path integral approach. The latter accommodates interactions on the dot in a numerically exact fashion. We apply the developed techniques to two open topics in nonequilibrium many-body physics: (i) We explore the role of many-body electron-electron repulsion effects on the dynamics of the system. Results, obtained using exact path integral simulations, are compared to mean-field quantum Langevin equation predictions. (ii) We analyze aspects of quantum equilibration and thermalization in large quantum systems using the probe technique, mimicking elastic-dephasing effects and inelastic interactions on the dot. Here, unitary simulations based on the fermionic trace formula are accompanied by quantum Langevin equation calculations.

## I. INTRODUCTION

There has been recently a great deal of interest in simulating the real-time dynamics of quantum systems, open or closed, prepared in a nonequilibrium state [1]. These investigations have been spurred by recent experimental breakthroughs in the ability to watch out-of-equilibrium dynamics, for example, in cold atomic gases [2], or in on-chip superconducting circuits [3]. This endeavor is fundamentally important for resolving basic issues in quantum dynamics, and in particular, for understanding equilibration and thermalization in quantum systems [1]. The nonequilibrium dynamics of the eminent Anderson model [4], composed of a single electronic level (quantum dot) coupled to two metals, has in particular been of great interest. This is because it is perhaps the simplest platform for probing both equilibrium and out-of-equilibrium physics in a many-body system. The model is integrable, even when electron-electron (e-e) repulsion effects are accounted for on the dot, and its integrability has been exploited for resolving its transport behavior [5].

A central strategy in most analytic and numerical tools devoted to the Anderson model, and impurity systems at large, is the separation of the total system into a subsystem (dot) and the environment (metals, referred to as reservoirs). The latter are typically assumed to be infinite-dissipative and are maintained in one of the canonical ensembles of statistical mechanics. This assumption allows one to treat the effect of the reservoirs on the subsystem within a self-energy term. However, once the reservoirs are traced out, one cannot describe their explicit dynamics. Among the numerical approaches developed along these lines we list the time-dependent numerical renormalization-group method [6], real-time diagrammatic Monte Carlo techniques [7] and path integral approaches [8, 9]. These methods place focus on quantities such as the dot occupancy, transmission probability, conductance, current, noise, and correlations on the *impurity*. The dynamics of the *total* system, including the electron reservoirs, has not yet been explored since general tools for simulating the overall dynamics in a system-bath scenario are still missing.

The current work develops analytical and numerical treatments of global system evolution based on established impurity dynamics techniques. These tools allow investigation of the roles of e-e interactions and decoherence and dissipation effects on nonequilibrium reservoirs dynamics. We focus on the finite-size Anderson model composed of two metallic grains weakly coupled through a single electronic level. We refer to the metal grains, each composed of  $N \sim 100 - 500$  electronic states and  $n \sim 50 - 200$  electrons as “reservoirs” alluding to their high density of states (DOS). This large DOS allows the reservoirs’ effect on the dot (subsystem) to be absorbed into a positive real self-energy function leading to a quantum Langevin equation (QLE) description [10–12], as we

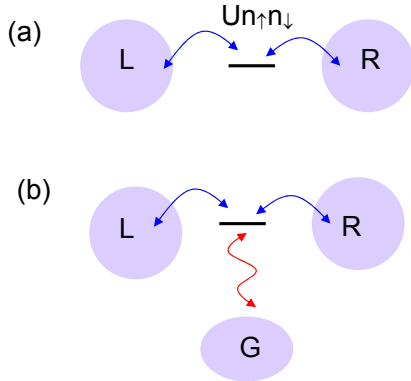


FIG. 1: Two metallic grains (reservoirs) separately prepared in a grand canonical- diagonal state. At  $t_0$  the reservoirs are put into contact through a single electronic state. We study three variants of this systems: a case without interactions, (a) allowing for electron repulsion effects on the dot only, and (b) accommodating decohering and inelastic effects on the dot, by coupling its electrons to a  $G$  reservoir, serving as a dephasing or a voltage probe.

explain below. A schematic representation is presented in Fig. 1. We are interested in following the real-time dynamics of *both* the dot and the reservoirs degrees of freedom. As an initial condition, we assume that each reservoir is prepared in a distinct Gibbs-like grand canonical state at a different chemical potential but at the same temperature.

In the absence of dephasing and inelastic effects, the dynamics of the total density matrix is followed by extending three approaches: (i) the quantum Langevin equation method [10–12], adopted here both in the noninteracting limit and in the mean-field (MF) regime, (ii) fermionic trace formula [13], used here for simulating the exact dynamics of the noninteracting model, and (iii) an influence functional path integral method [14, 15], employed to treat interactions beyond the perturbative regime. In the latter half of the paper, these techniques are used to study reservoir population evolution both without and with Coulomb repulsion effects on the dot, and in the presence of emulated dephasing and inelastic scattering effects.

While Coulomb interactions are explicitly introduced here, the inclusion of dephasing and inelastic effects warrants further discussion. The origin of such processes are many-body interactions in the system, e.g., electron phonon coupling. Since an explicit and exact inclusion of these interactions is extremely challenging [16–19], phenomenological techniques have been developed in their stand, [20–22]. In the case of elastic decohering processes the technique is referred to as a “dephasing probe”. In the case of inelastic scattering processes, it is referred to as a “voltage probe”. These probes are electron reservoirs, prepared such that, there is no either energy resolved

or total net electron flow from the  $L$ -dot- $R$  system towards these probes. For a scheme of this model, see Fig. 1(b). It should be noted that elastic-decohering processes or inelastic effects are only *emulated* here by the probes. The overall dynamics can be still simulated using the unitary trace formula technique [23]. We also extend the QLE method to include a probe, and time evolve the system. Since our calculations provide the real-time dynamics of the *full* density matrix (DM), the process of equilibration and thermalization in a finite quantum system can now be studied [23–26]. Particularly, we find that when only decoherence effects are allowed, the system approaches a non-canonical equilibrium state. In contrast, when inelastic processes are included, the reservoirs relax towards a common Gibbs-like state.

The paper is organized as follows. In Sec. II we present the finite-size closed Anderson model and outline the implementation of the probes. In Section III we present our developed numerical and analytic treatments of the density matrix dynamics: First, we extend the standard quantum Langevin equation approach to include reservoirs dynamics. The method can treat both the noninteracting model (III A 1), the case with interactions, only at the level of mean-field (Hartree) theory (III A 2), and the probe model (III A 3). Second, we present the fermionic trace formula, useful for studying the Anderson model without interactions and with implemented dephasing and inelastic effects in Sec. III B. The third method, presented in Sec. III C, is an influence-functional path integral approach [14, 15]. This non-perturbative tool can treat the model with interactions in a numerically exact manner. Applications are included in Sec. IV. The effects of Coulomb repulsion effects on the dot are studied using mean-field QLE and the path integral technique in Sec. IV A. In Sec. IV B quantum equilibration and thermalization is investigated using the probe technique. In this case, the total density matrix is resolved using the QLE method and the fermionic trace formula. The paper is summarized, along with an outlook, in Sec. V.

## II. MODEL

The closed-system Anderson model consists two metal grains,  $\nu = L, R$ , including (each) a collection of  $N_\nu$  dense electronic levels initially populated by noninteracting electrons up to the chemical potential  $\mu_\nu$ , at temperature  $T = \beta^{-1}$ . The two baths couple only through their (weak) hybridization with a single level quantum dot. Work presented in this study concerns three variants of the model. The simplest version is the “noninteracting case”, where electron-electron repulsion effects and any decohering and relaxation mechanisms are excluded. The second case, the “interacting model”, allows for e-e interactions on the dot only. The third model variant, the “probe

model”, phenomenologically contains elastic decohering and inelastic scattering processes on the dot, using the probe technique and excluding e-e repulsion effects. This model is discussed in detail in Sec. IV B, where it is applied in the context of quantum equilibration.

### A. The interacting model

In the absence of decoherence and dissipation effects the interacting Hamiltonian takes the form

$$H = H_L + H_R + H_W + \mathcal{V}_L + \mathcal{V}_R, \quad (1)$$

where  $H_{L,R,W}$  represents the Hamiltonian for the left reservoir, right reservoir and the dot, respectively. The term  $\mathcal{V}_\nu$  denotes the coupling of the dot to the  $\nu$  reservoir,

$$\begin{aligned} H_L &= \sum_{l,\sigma} \epsilon_l c_{l,\sigma}^\dagger c_{l,\sigma}, & H_R &= \sum_{r,\sigma} \epsilon_r c_{r,\sigma}^\dagger c_{r,\sigma} \\ \mathcal{V}_L &= \sum_{l\sigma} v_l c_{d,\sigma}^\dagger c_{l,\sigma} + h.c. & \mathcal{V}_R &= \sum_{r\sigma} v_r c_{d,\sigma}^\dagger c_{r,\sigma} + h.c. \\ H_W &= \sum_{\sigma} \epsilon_d c_{d,\sigma}^\dagger c_{d,\sigma} + U n_{d,\uparrow} n_{d,\downarrow}. \end{aligned} \quad (2)$$

Here,  $c_{k,\sigma}$  ( $k = l, r, d$ ) are fermionic operators of the left reservoir,  $l \in L$ , right reservoir,  $r \in R$  and the dot ( $d$ ). The symbol  $\sigma$  stands for the spin state ( $\uparrow$  or  $\downarrow$ ) and  $U$  accounts for the onsite repulsion energy. We assume that  $v_l$  and  $v_r$  are real numbers and that the Hamiltonians of the leads are diagonal in momentum basis and define the hybridization  $\Gamma_\nu(\epsilon) = \pi \sum_{k \in \nu} v_k^2 \delta(\epsilon - \epsilon_k)$ , taken in practice to be energy independent. The Hamiltonian (2) disregards magnetic fields, yielding spin-degenerate energy levels, thus it is sufficient to consider observables for one spin species. We note that the noninteracting case arises simply from the suppression of  $U$ .

Our objective in this paper is to calculate the time evolution of the expectation values of *all* two-body operators in the system ( $k, j = l, r, d$ )

$$\rho_{k,j}(t) \equiv \langle c_k^\dagger(t) c_j(t) \rangle \equiv \text{Tr}[\rho(t_0) c_k^\dagger(t) c_j(t)], \quad (3)$$

written here in the Heisenberg representation with  $\rho(t_0) = \rho_d \otimes \rho_L \otimes \rho_R$  representing the factorized time-zero density matrix of the system, and with the trace performed over all degrees of freedom. We suppress the spin degree of freedom in the density matrix since its elements are identical for the two spin configurations. As an initial condition, we take the dot to be empty and the reservoirs’ DM to be diagonal,

$$\langle c_d^\dagger(t_0) c_d(t_0) \rangle = 0, \quad \langle c_l^\dagger(t_0) c_l(t_0) \rangle = f_L(\epsilon_l) \equiv f_l, \quad \langle c_r^\dagger(t_0) c_r(t_0) \rangle = f_R(\epsilon_r) \equiv f_r, \quad (4)$$

with the population  $f_{L,R}(\epsilon) = [e^{\beta(\epsilon - \mu_{L,R})} + 1]^{-1}$ . As a convention, we use the symmetric chemical potential bias  $\mu_L = -\mu_R > 0$ .

## B. The probe model

The Anderson probe model, a variant of the basic model, Eq. (2), can emulate memory loss and energy redistribution in a quantum system without explicitly introducing many-body interactions [20–22]. The probe technique has been of extensive use in mesoscopic physics, for describing the disappearance of quantum effects in transport [21], dissipation [20], and equilibration dynamics [27]. Recent advances include a full-counting statistics analysis of the probe model [28], and an extension of the probe technique to the AC regime [29]. We model here either a dephasing probe, allowing for quasi-elastic decoherence processes, or a voltage probe, where inelastic effects are further mimicked. In both cases we suppress electron-electron interaction effects in the system.

As we explain next, in our study the “probe” terminology refers to a setup slightly different from the conventional one. The standard construction refers to an open system scenario, where the probe practically performs which-path experiments through repetitive measurements of the system [30]. In contrast, in our picture the probe is a finite-closed quantum system, only *initialized* with a certain-special distribution. After its preparation, the probe, similarly to other parts of the system, is left undisturbed. Thus, we can use exact unitary approaches and simulate the dynamics of the total system. While this picture abuses to some extent the standard notion of a “probe”, we maintain this terminology here since practically our implemented probe acts like a proper one, inducing phase loss or/and energy reorganization in the system.

We introduce a probe into the model by adding an additional Fermi-sea reservoir, denoted by the letter  $G$ , to the Hamiltonian (2), again discarding the spin degree of freedom,

$$H_P = H + H_G + \mathcal{V}_G, \quad (5)$$

where

$$H_G = \sum_g \epsilon_g c_g^\dagger c_g, \quad \mathcal{V}_G = \sum_g v_g c_g^\dagger c_d + h.c. \quad (6)$$

We naturally define the hybridization  $\Gamma_G(\epsilon) = \pi \sum_g v_g^2 \delta(\epsilon - \epsilon_g)$ , and take it as a constant. As always, our objective here is the resolution of all system expectation values of two-body operators ( $k, j = l, r, d$ ),  $\rho_{k,j}(t)$ . As initial conditions we assume Eq. (4), where the  $G$  bath initial condition is set according to the particular probe condition, explained below.

*Voltage probe.* Inelastic scattering effects of electrons on the dot are effectively included by implementation of a voltage probe. The probe has a canonical distribution,  $f_G(\epsilon) = [e^{\beta(\epsilon - \mu_G)} + 1]^{-1}$ , and its chemical potential  $\mu_G$  is set such that the net charge current from the dot to the  $G$  unit vanishes for all times

$$i_G \equiv \frac{d}{dt} \sum_g \langle c_g^\dagger c_g \rangle = 0. \quad (7)$$

With the motivation to explore situations beyond the linear response regime [31], we retrieve  $\mu_G$  numerically, by employing the Newton-Raphson method [32],

$$\mu_G^{(m+1)} = \mu_G^{(m)} - i_G(\mu_G^{(m)})/i'_G(\mu_G^{(m)}). \quad (8)$$

$\mu_G^{(0)}$  is the initial guess,  $i'_G$  denotes the first derivative with respect to  $\mu_G$ . In principle, one should adjust  $\mu_G$  throughout the simulation, to eliminate population leakage from the  $L$ -dot- $R$  system into  $G$ . However, we have found in our simulations that the  $G$  bath has lawfully behaved as a probe once we determined  $\mu_G$  from the steady-state limit using the following analytic expression for the charge current

$$i_G(\epsilon) = \frac{2\Gamma_G \Gamma_R [f_G(\epsilon) - f_R(\epsilon)] + \Gamma_L [f_G(\epsilon) - f_L(\epsilon)]}{\pi (\epsilon - \epsilon_d)^2 + \Gamma^2},$$

$$i_G = \int i_G(\epsilon) d\epsilon, \quad (9)$$

with  $\Gamma = \Gamma_L + \Gamma_R + \Gamma_G$  [33]. The lower and upper integration limits are determined by the band simulated. Substituting Eq. (9) in Eq. (7), a voltage probe condition is set by demanding  $f_G(\epsilon)$  to fulfill the relation

$$\int d\epsilon \frac{f_G(\epsilon)}{(\epsilon - \epsilon_d)^2 + \Gamma^2} = \frac{1}{\Gamma_L + \Gamma_R} \int d\epsilon \frac{f_L(\epsilon)\Gamma_L + f_R(\epsilon)\Gamma_R}{(\epsilon - \epsilon_d)^2 + \Gamma^2}. \quad (10)$$

*Dephasing probe.* Implementation of the dephasing probe, fabricating elastic decoherence, necessitates the stronger requirement  $i_G(\epsilon) = 0$ , i.e., the charge current at a given energy should vanish. Using the steady-state behavior (9), we obtain a non-Fermi distribution

$$f_G(\epsilon) = \frac{\Gamma_R f_R(\epsilon) + \Gamma_L f_L(\epsilon)}{\Gamma_R + \Gamma_L}. \quad (11)$$

We emphasize that  $\mu_G$  or  $f_G$  have been determined here in the steady-state limit, assuming fixed chemical potentials for the  $L$  and  $R$  baths. Indeed, at short time,  $\Gamma_{L,R}t \lesssim 2$ , before a (quasi) steady-state sets in, we find that  $i_G \neq 0$ . However, we have confirmed numerically that beyond this time throughout all our simulations  $|i_G/i_{L,R}| < 10^{-4}$ , thus the  $G$  reservoir plays the role of a proper probe.

Three different approaches for the calculation of the full DM are described in Sections III A, III B and III C. Applications are included in Sec. IV.

### III. METHODS

#### A. Quantum Langevin Equation

The dynamics of the Anderson model in the absence of interactions ( $U = 0$ ), with interactions at the mean-field level, or with a probe, is described here within a quantum Langevin equation framework [10]. The basis of our method has been used in the past to follow the dot evolution or the charge and energy currents in the system [11, 12]. Here, we show results for the full DM. We begin our analysis with the trivial treatment of the impurity (dot) and review the steps involved. This review helps highlight underlying approximations and establishes limits for the method's applicability.

##### 1. Noninteracting case ( $U = 0$ )

In the Heisenberg representation the fermionic operators satisfy the following equations of motion (EOM),

$$\begin{aligned}\dot{c}_d &= -i\epsilon_d c_d - i \sum_l v_l c_l - i \sum_r v_r c_r \\ \dot{c}_l &= -i\epsilon_l c_l - i v_l c_d \\ \dot{c}_r &= -i\epsilon_r c_r - i v_r c_d\end{aligned}\tag{12}$$

Formal integration of the reservoirs EOM yields, e.g. at the  $L$  end,

$$c_l(t) = e^{-i\epsilon_l(t-t_0)} c_l(t_0) - i v_l \int_{t_0}^t d\tau e^{-i\epsilon_l(t-\tau)} c_d(\tau) d\tau.\tag{13}$$

We substitute Eq. (13), and the analogous expression for  $c_r(t)$ , into the dot EOM [Eq. (12)], and retrieve

$$\begin{aligned}\dot{c}_d &= -i\epsilon_d c_d - i \sum_l v_l e^{-i\epsilon_l(t-t_0)} c_l(t_0) - i \sum_r v_r e^{-i\epsilon_r(t-t_0)} c_r(t_0) \\ &\quad - \int_{t_0}^t d\tau \sum_l v_l^2 e^{-i\epsilon_l(t-\tau)} c_d(\tau) - \int_{t_0}^t d\tau \sum_r v_r^2 e^{-i\epsilon_r(t-\tau)} c_d(\tau).\end{aligned}\tag{14}$$

In this (exact) equation the second and third terms are interpreted as “noise” [10],

$$\begin{aligned}\eta^L(t) &\equiv \sum_l v_l e^{-i\epsilon_l(t-t_0)} c_l(t_0) \\ \eta^R(t) &\equiv \sum_r v_r e^{-i\epsilon_r(t-t_0)} c_r(t_0).\end{aligned}\tag{15}$$



The last two terms in Eq. (14) can be reduced, each, into decay terms, further inducing an energy shift of the dot energy, absorbed into the definition of  $\epsilon_d$ . This is justified by following two assumptions: (i) The hybridization  $\Gamma_\nu(\epsilon) = \pi \sum_{k \in \nu} v_k^2 \delta(\epsilon - \epsilon_k)$  may be taken as a positive real self-energy function [10], and (ii) the dot dynamics is slow relative to the reservoirs' evolution. We now explain the steps involved. First, we define a new operator for the dot, by absorbing its fast oscillatory behavior,  $\tilde{c}_d(t) \equiv c_d e^{i\epsilon_d t}$ . Its EOM is

$$\dot{\tilde{c}}_d = -i[\eta_L(t) + \eta_R(t)]e^{i\epsilon_d t} - \int_{t_0}^t d\tau \sum_l v_l^2 e^{-i\epsilon_{ld}(t-\tau)} \tilde{c}_d(\tau) - \int_{t_0}^t d\tau \sum_r v_r^2 e^{-i\epsilon_{rd}(t-\tau)} \tilde{c}_d(\tau) \quad (16)$$

where  $\epsilon_{kj} \equiv \epsilon_k - \epsilon_j$ . We then change variables,  $x \equiv t - \tau$ , and make the assumption that the dot evolution (now missing the fast phase oscillation) is slow with respect to other time scales in the system,  $\tilde{c}_d(t-x) \sim \tilde{c}_d(t)$ . This results in

$$\int_{t_0}^t d\tau \sum_l v_l^2 e^{-i\epsilon_{ld}(t-\tau)} \tilde{c}_d(\tau) \approx \tilde{c}_d(t) \sum_l v_l^2 \int_0^{t-t_0} e^{-i\epsilon_{ld}x} dx$$

If the time is long,  $t \gg t_0$ , integration gives

$$\sum_l v_l^2 \int_0^{t-t_0} e^{-i\epsilon_{ld}x} dx = \Gamma_L(\epsilon_d) - 2iv_l^2 \lim_{t \rightarrow \infty} \left[ \int_{-\infty}^{+\infty} D_L(\epsilon) \frac{\sin^2(\epsilon - \epsilon_d)t}{\epsilon - \epsilon_d} d\epsilon \right]$$

with  $D_L(\epsilon) = \sum_l \delta(\epsilon - \epsilon_l)$  as the density of states of the  $L$  metal, taken as flat here. We also take the interaction parameters  $v_l$  to be independent of the  $l$  index. The imaginary term introduces an energy shift, which can be absorbed into the definition of  $\epsilon_d$ . It diminishes when the density of states does not depend on energy (the case used later), and when the bandwidth is large enough. In our numerical calculations we have used a finite bandwidth with a cutoff  $D = \pm 1$ , introducing a small correction to  $\epsilon_d$ . We return to Eq. (14) and conclude that it obeys the quantum Langevin equation

$$\dot{c}_d = -i\epsilon_d c_d - i\eta^L(t) - i\eta^R(t) - \Gamma(\epsilon_d) c_d(t), \quad (17)$$

with  $\Gamma(\epsilon) = \Gamma_L(\epsilon) + \Gamma_R(\epsilon)$ . The dynamics of the dot occupation,  $\langle n_d(t) \rangle$ , can be reached by a formal integration of Eq. (17),

$$c_d(t) = c_d(t_0) e^{(-i\epsilon_d - \Gamma)(t-t_0)} - i \int_{t_0}^t e^{(-i\epsilon_d - \Gamma)(t-\tau)} [\eta^L(\tau) + \eta^R(\tau)] d\tau, \quad (18)$$

to provide the standard expression [34]

$$\langle n_d(t) \rangle \equiv \langle c_d^\dagger(t) c_d(t) \rangle = \sum_{k=l,r} \frac{|v_k|^2 f_k}{\epsilon_{dk}^2 + \Gamma^2} \left[ 1 + e^{-2\Gamma(t-t_0)} - 2e^{-\Gamma(t-t_0)} \cos[\epsilon_{dk}(t-t_0)] \right]. \quad (19)$$

This derivation relied on the initial conditions (4). The summation runs over all the reservoirs degrees of freedom [35]. We now use Eq. (13) and its analogous expression for  $c_r(t)$ , together with Eq. (18), and derive analytical expressions for other quadratic expectation values,  $\langle c_k^\dagger(t)c_j(t) \rangle$ ,  $k, j = l, r, d$ . These results are valid as long as one can faithfully rely on Eq. (17). In what follows we take  $t_0 = 0$  to simplify our notation. The reservoir-dot coherence can be obtained analytically,

$$\rho_{d,l}(t) \equiv \langle c_d^\dagger(t)c_l(t) \rangle = B_1 + B_2. \quad (20)$$

Here,  $B_1$  includes contributions from the  $L$  side only,

$$B_1 = \frac{iv_l f_l}{\Gamma - i\epsilon_{dl}} \left[ 1 - e^{-t(\Gamma - i\epsilon_{dl})} \right]. \quad (21)$$

$B_2$  includes electron transmission pathways from the  $L$  side, through the dot, to the  $K = L, R$  grain,

$$B_2 = -iv_l \sum_{k \in L, R} \frac{v_k^2 f_k}{\Gamma^2 + \epsilon_{dk}^2} \times \left\{ \frac{1 - e^{i\epsilon_{kl}t}}{i\epsilon_{lk}} + \frac{e^{-2\Gamma t} - e^{-t(\Gamma - i\epsilon_{dl})}}{i\epsilon_{ld} - \Gamma} - \frac{e^{-t(\Gamma - i\epsilon_{kd})} - e^{-i\epsilon_{lk}t}}{i\epsilon_{ld} - \Gamma} - \frac{e^{-t(\Gamma - i\epsilon_{dk})} - e^{-t(\Gamma + i\epsilon_{ld})}}{i\epsilon_{lk}} \right\}. \quad (22)$$

Using Eq. (20), we derive an expression for the charge current at the  $L$  contact,

$$\begin{aligned} i_L(t) &\equiv \frac{d}{dt} \sum_l \langle c_l^\dagger(t)c_l(t) \rangle = -2\Im \sum_l v_l \langle c_d^\dagger(t)c_l(t) \rangle \\ &= \frac{2\Gamma_L \Gamma_R}{\pi} \sum_l \frac{f_L - f_R}{\epsilon_{ld}^2 + \Gamma^2} - \frac{2\Gamma_L}{\pi} e^{-\Gamma t} \sum_l \frac{1}{\epsilon_{ld}^2 + \Gamma^2} \\ &\times \left\{ e^{-\Gamma t} (f_l \Gamma_L + f_r \Gamma_R) - (2f_l \Gamma_L + 2f_r \Gamma_R - \Gamma f_l) \cos(\epsilon_{ld}t) - f_l \epsilon_{ld} \sin(\epsilon_{ld}t) \right\}. \end{aligned} \quad (23)$$

Here  $\Im$  stands for the imaginary part. An analogous expression can be written for  $i_R(t)$ . Ref. [34] includes a Green's function based derivation for the time dependent current in the symmetric limit ( $\Gamma_L = \Gamma_R$ ). This derivation results in a surplus nonphysical term at the initial time. We now turn our attention to the reservoirs' states population. Using Eq. (13), we find that it is given by three contributions,

$$\begin{aligned} p(\epsilon_l) &\equiv \langle c_l^\dagger(t)c_l(t) \rangle = \langle c_l^\dagger(t_0)c_l(t_0) \rangle \\ &+ iv_l e^{-i\epsilon_l(t-t_0)} \int_{t_0}^t e^{i\epsilon_l(t-\tau)} \langle c_d^\dagger(\tau)c_l(t_0) \rangle d\tau + c.c. \\ &+ v_l^2 \int_{t_0}^t \int_{t_0}^t d\tau_1 d\tau_2 \langle c_d^\dagger(\tau_1)c_d(\tau_2) \rangle e^{i\epsilon_l(t-\tau_1)} e^{-i\epsilon_l(t-\tau_2)}. \end{aligned} \quad (24)$$

The two-times correlation functions can be obtained from Eqs. (13) and (18) without additional approximations, and the explicit expressions are given in Appendix A. Similarly, closed analytic expressions can be written for inter and intra-reservoir coherences, e.g.  $\rho_{l,k}(t)$ ,  $k \in L, R$ , see Appendix A. Eqs. (19), (20), (24), (A3) and (A4), and the analogous  $R$ -bath expressions, form the time-dependent full density matrix of the system.

*Timescales.* We now comment on the applicability of the QLE approach. Given infinite reservoirs, a current carrying steady-state behavior develops, and the dot occupation, as well as the charge current, reach a fixed value after a short time,  $\tau_t \gtrsim 2/\Gamma$  (see for example Fig. 8). However, since the reservoirs are finite in the present treatment, recurrence effects should eventually manifest in our system. These effects cannot be handled by the QLE technique since an *irreversible* behavior has been assumed for the dot, as Eq. (17) breaks unitary evolution. The technique can still excellently reproduce the exact dynamics in the so called “quasi steady-state” (QSS) region, up to  $\tau_d \sim 2\pi N/D$  [36]. Here  $N$  is the number of electronic states in each bath and  $D$  is the band cutoff. Within this time, the dot occupation and the charge current are constant, similar to a real steady-state situation. Around the time  $\tau_d$  the dot occupation should begin to vary, showing (partial) recurrence behavior, and the QSS limit breaks down.

Fig. 2 clarifies this timescale issue. The left panel displays the dot occupation as a function of time using either the QLE approach (full line) or an exact method (dashed line), described in Sec. III B. Results agree up to  $t \sim \tau_d \sim 630$ , and deviations before this time are due to the finite band used in QLE, while neglecting the energy correction in Eq. (17). Around the time  $\tau_d$  exact simulations show a partial reversal of the dot occupation, while QLE still produces the QSS value. At a later time,  $t \gg \tau_d$ , the QLE data diverges. Panel (b) presents the bath occupation for two selected energies, and we find that nonphysical values, such as a population exceeding unity, can be obtained with QLE when  $t > \tau_d$ . Thus, the QLE method can be used within the interval  $t < \tau_d$  only, to be consistent with its underlying assumptions. However, interesting nonequilibrium physics takes place within this window, thereby making this approach valuable considering that exact computational schemes are very expensive.

## 2. Mean-field theory

The QLE description of Sec. III A 1 can be generalized to accommodate electron-electron repulsion effects on the dot at the mean-field level. We refer to this extension as a MF QLE treatment, and note that it is not trivial: While a MF theory has been developed, suffering from some patholo-

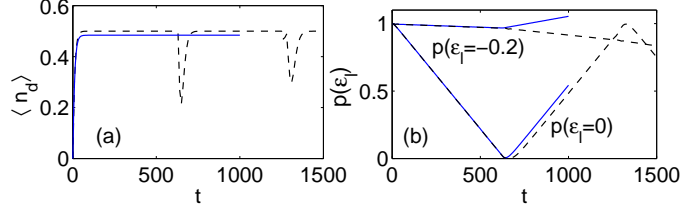


FIG. 2: (a) Dot occupation as a function of time calculated using either the QLE method (full line) or the trace formula (dashed line), described in Sec. III B. (b) Population of two selected states of the left reservoir, plotted as a function of time,  $\epsilon_l = -0.2$  (top) and  $\epsilon_l = 0$  (bottom). In both cases we simulated the noninteracting Anderson model with  $\epsilon_d = 0$ ,  $\mu_L = -\mu_R = 0.2$ ,  $\Gamma_L = \Gamma_R = 0.025$  and  $\Gamma_G = 0$ ,  $N_{L,R}=201$  and  $D = \pm 1$ .

gies, for the study of dot occupation or charge current in the steady-state limit [37, 38], here we present a MF scheme to describe the *real-time dynamics* of the *full density matrix*. By comparing MF results to exact numerical simulations, see Sec. IV, we conclude that a MF description can produce physical results up to  $\frac{U}{\Gamma}, \frac{U}{\mu_L - \mu_R} \lesssim O(1)$ . The effectiveness of the method also delicately depends on the dot level position, see for example Fig. 7.

The MF prescription, treating Coulombic repulsion, takes us back to Eq. (2). We now assume that the many-body interaction term can be factorized [37, 38]

$$U n_{d,\uparrow} n_{d,\downarrow} \rightarrow U [\langle n_{d,\uparrow} \rangle n_{d,\downarrow} + n_{d,\uparrow} \langle n_{d,\downarrow} \rangle]. \quad (25)$$

This assumption reduces the Hamiltonian to an effectively noninteracting one, with a renormalized dot energy

$$\tilde{\epsilon}_d(t) = \epsilon_d + U \langle n_d(t) \rangle. \quad (26)$$

The spin-index has been dropped here, as we choose not to study magnetic effects. The formalism could be feasibly generalized to include magnetic fields, resulting in  $\epsilon_{d,\uparrow} \neq \epsilon_{d,\downarrow}$ . In such situations the validity of MF equations is governed by another energy scale besides  $U/\Gamma$  and  $U/\Delta\mu$ , namely  $U/(\epsilon_{d,\uparrow} - \epsilon_{d,\downarrow})$ . The dot occupation is determined in a self-consistent manner at every instant by modifying Eq. (19) to contain the dot renormalized energy,

$$\langle n_d(t) \rangle = \sum_{k=l,r} \frac{|v_k|^2 f_k}{[\epsilon_{dk} + U \langle n_d(t) \rangle]^2 + \Gamma^2} \left[ 1 + e^{-2\Gamma t} - 2e^{-\Gamma t} \cos[(\epsilon_{dk} + U \langle n_d(t) \rangle)t] \right]. \quad (27)$$

The solution provides the renormalized dot energy  $\tilde{\epsilon}_d(t)$ , which is then used to replace  $\epsilon_d$  in Eqs. (20), (24), (A3) and (A4), to provide the full DM at the MF level.

### 3. Probe model

To implement elastic dephasing or inelastic effects with a probe, the set of equations (12) is augmented by an additional equation for  $c_g$ . The EOM for  $c_d$  must be modified to include its coupling to the  $G$  bath,

$$\begin{aligned}\dot{c}_g &= -i\epsilon_g c_g - iv_g c_d \\ \dot{c}_d &= -i\epsilon_d c_d - i \sum_l v_l c_l - i \sum_r v_r c_r - i \sum_g v_g c_g.\end{aligned}\quad (28)$$

It can be easily shown that under the QLE basic assumptions, as discussed in Sec. III A 1, the dot still satisfies Eq. (17) with an additional noise term  $\eta^G$  and with a re-defined total hybridization,  $\Gamma = \Gamma_L + \Gamma_R + \Gamma_G$ . The noise  $\eta^G$  obeys a relation analogous to Eq. (15), and Eq. (18) is generalized to

$$c_d(t) = c_d(t_0) e^{(-i\epsilon_d - \Gamma)(t-t_0)} - i \int_{t_0}^t e^{(-i\epsilon_d - \Gamma)(t-\tau)} [\eta^L(\tau) + \eta^R(\tau) + \eta^G(\tau)] d\tau. \quad (29)$$

We can now recognize that, in the presence of the probe, the expressions for the DM elements (19), (20), (24), (A3) and (A4) stay formally intact. The technical adjustments are as follows: (i) We re-define the total hybridization,  $\Gamma = \Gamma_L + \Gamma_R + \Gamma_G$ . (ii) We augment summations that run over both  $L$  and  $R$  baths by  $k \in G$  terms. For example, the summation in  $F_3$  [Eq. (A2)] should include such terms. (iii) We set the  $G$  bath distribution to satisfy the probe conditions, explained in Sec. II.

#### B. Fermionic trace formula ( $U = 0$ )

We describe here an exact brute force calculation that can provide numerically all the elements of the density matrix in the noninteracting case. We begin without the presence of a probe, opting to include its effects later. This unitary method complements the QLE description, whose validity is governed by  $\tau_d$ . Since the method is unitary, a recurrences behavior is expected to manifest at long enough time. The core of the method is the trace formula for fermions [13]

$$\text{Tr} [e^{M_1} e^{M_2} \dots e^{M_p}] = \det [1 + e^{m_1} e^{m_2} \dots e^{m_p}], \quad (30)$$

where  $m_p$  is a single-particle operator corresponding to a quadratic operator  $M_p = \sum_{i,j} (m_p)_{i,j} c_i^\dagger c_j$ .  $c_i^\dagger$  ( $c_j$ ) are fermionic creation (annihilation) operators. Our objective is the dynamics of a quadratic operator  $A$ , either given by system or bath degrees of freedom,  $A \equiv c_j^\dagger c_k$ ,  $j, k = l, r, d$ ,

$$\langle A(t) \rangle = \text{Tr} [\rho(t_0) e^{iHt} A e^{-iHt}] = \lim_{\lambda \rightarrow 0} \frac{\partial}{\partial \lambda} \text{Tr} [\rho_L \rho_R \rho_d e^{iHt} e^{\lambda A} e^{-iHt}]. \quad (31)$$

We introduce the  $\lambda$  parameter, taken to vanish at the end of the calculation. The initial condition is taken to be factorized,  $\rho(t_0) = \rho_d \otimes \rho_L \otimes \rho_R$ ,  $\rho_\nu = e^{-\beta(H_\nu - \mu_\nu N_\nu)} / Z_\nu$ ,  $Z_\nu$  is the partition function,  $\rho_d$  describes the dot initial density matrix. These density operators follow an exponential form,  $e^M$ , with  $M$  a quadratic operator. The application of the trace formula leads to

$$\langle e^{\lambda A(t)} \rangle = \det \left\{ [I_L - f_L] \otimes [I_R - f_R] \otimes [I_d - f_d] + e^{iht} e^{\lambda a} e^{-iht} f_L \otimes f_R \otimes f_d \right\}. \quad (32)$$

Here,  $a$  and  $h$  are single-body matrices of the  $A$  and  $H$  operators, respectively. The matrices  $I_\nu$  and  $I_d$  are the identity matrices for the  $\nu = L, R$  space and for the dot. The functions  $f_L$  and  $f_R$  are the band electrons occupancy  $f_\nu(\epsilon) = [e^{\beta(\epsilon - \mu_\nu)} + 1]^{-1}$ . Here they are written in matrix form and in the energy representation.  $f_d$  represents the dot initial occupation, again written in a matrix form. Since we are working with finite-size reservoirs, Eq. (32) can be readily simulated numerically-exactly.

The fermionic trace formula can be trivially generalized to include a probe. We add the  $G$  bath into the expectation value expression,  $A \equiv c_j^\dagger c_k$ ,

$$\langle A(t) \rangle = \text{Tr} [\rho(t_0) e^{iH_P t} A e^{-iH_P t}] = \lim_{\lambda \rightarrow 0} \frac{\partial}{\partial \lambda} \text{Tr} \left[ \rho_L \rho_R \rho_G \rho_d e^{iH_P t} e^{\lambda A} e^{-iH_P t} \right], \quad (33)$$

where as before  $\rho_\nu = e^{-\beta(H_\nu - \mu_\nu N_\nu)} / Z_\nu$ ,  $Z_\nu$  is the partition function,  $\nu = L, R, G$ .  $\rho_d$  stands for the dot initial density matrix, and we trace over all DOF, the two reservoirs, the probe, and the dot.

*Timescales.* Simulations with the trace formula are not restricted to a certain time scale. The method is unitary, providing (physical) recurrence behavior due to finite size effects. Since the time evolution scheme is not iterative, the accuracy of results does not deteriorate in time.

### C. Numerically exact path integral simulations, $U \neq 0$

The time evolution of the closed and *interacting* Anderson model can be simulated by employing a numerically-exact iterative influence-functional path integral (INFPI) approach [14, 15]. This method relies on the fact that in out-of-equilibrium (and nonzero temperature) cases bath correlations have a finite range, allowing for their truncation beyond a memory time dictated by the voltage-bias and the temperature. Based on this finite-memory assumption, an iterative-deterministic time-evolution scheme has been developed, where convergence with respect to the memory length can, in principle, be reached. The principles of the INFPI approach have been detailed in Refs. [14, 15], where it has been developed to investigate dissipation effects in the nonequilibrium spin-fermion model, and the population and current dynamics in correlated quantum dots. Recently, it has been used to examine the effects of a magnetic flux on the intrinsic

coherence dynamics in an Aharonov-Bohm quantum dot interferometer [39]. The INFPI method relies on the existence of a finite decorrelation time, thus it is suited for simulating the dynamics of an impurity coupled to a bath. Here we show that it can be used to retrieve the total DM in a system-bath setup. While in principle the method could encompass both interactions and probe, we focus exclusively on the first element.

The method is based on the fermionic trace formula (30), incorporating many-body effects within a path integral expression. Our work starts with the time evolution expression (31) under the Hamiltonian (2). We factorize the time evolution operator,  $e^{iHt} = (e^{iH\delta t})^{N_t}$ ,  $N_t\delta t = t$ , and adopt the Trotter decomposition  $e^{iH\delta t} \approx (e^{iH_0\delta t/2}e^{iH_1\delta t}e^{iH_0\delta t/2})$ , where  $H = H_0 + H_1$  with

$$\begin{aligned} H_0 &= \sum_{\nu=L,R} (H_\nu + \mathcal{V}_\nu) + \sum_{\sigma} \left( \epsilon_d + \frac{U}{2} \right) c_{d,\sigma}^\dagger c_{d,\sigma} \\ H_1 &= U \left[ n_{d,\uparrow} n_{d,\downarrow} - \frac{1}{2} (n_{d,\uparrow} + n_{d,\downarrow}) \right]. \end{aligned} \quad (34)$$

$H_1$  extracts many-body interactions on the dot, and it is eliminated by introducing auxiliary Ising variables  $s = \pm$  via the Hubbard-Stratonovich (HS) transformation [40],

$$e^{\pm iH_1\delta t} = \frac{1}{2} \sum_s e^{H_\pm(s)}, \quad e^{H_\pm(s)} \equiv e^{-s\kappa_\pm(n_{d,\uparrow} - n_{d,\downarrow})}. \quad (35)$$

Here,  $\kappa_\pm = \kappa' \mp i\kappa''$ ,  $\kappa' = \sinh^{-1}[\sin(\delta t U/2)]^{1/2}$ ,  $\kappa'' = \sin^{-1}[\sin(\delta t U/2)]^{1/2}$ . The uniqueness of this transformation requires that  $U\delta t < \pi$ . Incorporating the Trotter decomposition and the HS transformation into Eq. (31), we find that the time evolution of  $A$  is dictated by

$$\langle A(t) \rangle = \lim_{\lambda \rightarrow 0} \frac{\partial}{\partial \lambda} \left\{ \int ds_1^\pm ds_2^\pm \dots ds_{N_t}^\pm I(s_1^\pm, s_2^\pm, \dots, s_{N_t}^\pm) \right\}. \quad (36)$$

The integrand, referred to as the ‘‘Influence Functional’’ (IF), is given by ( $q = 1$ ,  $q + p = N_t$ )

$$I(s_q^\pm, \dots, s_{q+p}^\pm) = \frac{1}{2^{2(p+1)}} \text{Tr} \left[ \rho(t_0) \mathcal{G}_+(s_{q+p}^+) \dots \mathcal{G}_+(s_q^+) e^{iH_0(q-1)\delta t} e^{\lambda A} e^{-iH_0(q-1)\delta t} \mathcal{G}_-(s_q^-) \dots \mathcal{G}_-(s_{q+p}^-) \right], \quad (37)$$

where  $\mathcal{G}_+(s_q^+) = (e^{iH_0\delta t/2} e^{H_+(s_q^+)} e^{iH_0\delta t/2})$  and  $\mathcal{G}_- = \mathcal{G}_+^\dagger$ . Eq. (36) is exact in the  $\delta t \rightarrow 0$  limit. Practically, it is evaluated by truncating the IF beyond a memory time  $\tau_c = N_s\delta t$ , corresponding to the time beyond which bath correlations may be ignored [15],  $N_s$  is an integer. The following (non-unique) breakup has been suggested by [15],

$$I(s_1^\pm, s_2^\pm, \dots, s_{N_t}^\pm) \simeq I(s_1^\pm, s_2^\pm, \dots, s_{N_s}^\pm) I_s(s_2^\pm, s_3^\pm, \dots, s_{N_s+1}^\pm) \dots I_s(s_{N_t-N_s+1}^\pm, s_{N_t-N_s+2}^\pm, \dots, s_{N_t}^\pm), \quad (38)$$

where each element in the product, besides the first one, is given by a ratio between truncated IFs,

$$I_s(s_q, s_{q+1}, \dots, s_{q+N_s-1}) = \frac{I(s_q^\pm, s_{q+1}^\pm, \dots, s_{q+N_s-1}^\pm)}{I(s_q^\pm, s_{q+1}^\pm, \dots, s_{q+N_s-2}^\pm)}. \quad (39)$$

We now define a multi-time object,

$$\begin{aligned} & \mathcal{R}(s_{q+1}^\pm, s_{q+2}^\pm, \dots, s_{q+N_s-1}^\pm) \\ & \equiv \sum_{s_1^\pm, s_2^\pm, \dots, s_q^\pm} I(s_1^\pm, s_2^\pm, \dots, s_{N_s}^\pm) I_s(s_2^\pm, s_3^\pm, \dots, s_{N_s+1}^\pm) \dots \times I_s(s_q^\pm, s_{q+1}^\pm, \dots, s_{q+N_s-1}^\pm), \end{aligned} \quad (40)$$

and evolve it iteratively by multiplication with the subsequent truncated IF, followed by summation over the time variables at the head,

$$\mathcal{R}(s_{q+2}^\pm, s_{q+3}^\pm, \dots, s_{q+N_s}^\pm) = \sum_{s_{q+1}^\pm} \mathcal{R}(s_{q+1}^\pm, s_{q+2}^\pm, \dots, s_{q+N_s-1}^\pm) I_s(s_{q+1}^\pm, s_{q+2}^\pm, \dots, s_{q+N_s}^\pm). \quad (41)$$

The behavior at a particular time  $t_q$  is reached by summation over the internal variables,

$$\langle e^{\lambda A(t_q)} \rangle = \sum_{s_{q+2-N_s}^\pm, \dots, s_q^\pm} \mathcal{R}(s_{q+2-N_s}^\pm, s_{q+3-N_s}^\pm, \dots, s_q^\pm). \quad (42)$$

This procedure is repeated for several (small) values of  $\lambda$ , and the expectation value  $\langle A(t_q) \rangle$  is retrieved by numerical differentiation in  $\lambda$ . The truncated IF, Eq. (37), is the core of this calculation. It is achieved numerically-exactly using the fermionic trace formula (30).

*Timescale.* Previous studies for dense reservoirs have confirmed that INFPI can provide accurate results in both short time and in the quasi steady-state region [14, 15]. However, the method is not restricted to such dense-reservoirs situations, and it can describe the dynamics of small metallic grains since it handles all states explicitly. It should be still noted that the basic working assumption behind INFPI is the existence of a finite bath-induced decorrelation time. If the metal grains are very small, including few discrete states, this memory time  $\tau_c$  does not exist or it becomes large, hindering convergence. Roughly, one could expect that a decorrelation time can be identified when a system-bath picture still holds, in the sense that a QLE description can be written i.e., Eq. (17) is valid. In such situations, INFPI simulations should converge and generally hold beyond  $\tau_d$ . In practice, since these calculations are intensive, we have computed dynamics within a relatively short interval,  $\Gamma t < 5$ , where the QSS description is still valid.

#### IV. APPLICATIONS

We now turn our attention to applications of the preceding methods. We first study the effects of Coulombic interactions on the reservoirs' DOF evolution. We later investigate the equilibration process in the system, through the implementation of probes.



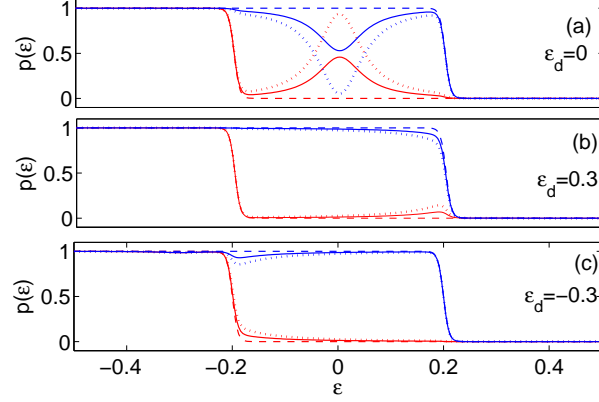


FIG. 3: Population of reservoirs' levels in the noninteracting case with the dot energy positioned (a) within the bias window at  $\epsilon_d = 0$ , (b) above the bias window at  $\epsilon_d = 0.3$ , and (c) below it at  $\epsilon_d = -0.3$ . Plotted are the  $L$  (three top lines) and  $R$  (three bottom lines) occupations as a function of electron energy, at  $\Gamma t = 0$  (dashed)  $\Gamma t = 9.5$  (full) and  $\Gamma t = 19$  (dotted). The framework used is a quantum Langevin approach (Sec. III A) with  $\beta = 200$  for the inverse temperature,  $\Gamma_L = \Gamma_R = 0.025$  for bath-dot hybridization,  $\Gamma = \Gamma_L + \Gamma_R$ ,  $\mu_L = -\mu_R = 0.2$  as a symmetric bias. The reservoirs are modeled by flat bands with a sharp cutoff at  $D = \pm 1$ , including  $N = 501$  electronic states for each reservoir.

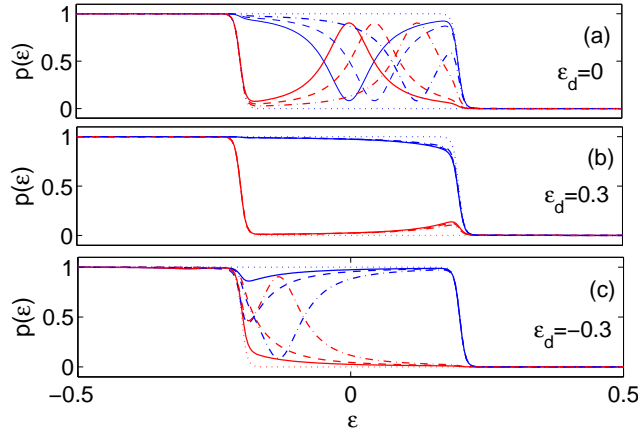


FIG. 4: Population of reservoirs' states from a mean-field QLE treatment. Plotted are the  $L$  (three top lines) and  $R$  (three bottom lines) occupations as a function of electron energy at  $\Gamma t = 15$  using the same set of parameters as in Fig. 3. (a)  $\epsilon_d = 0$ , (b)  $\epsilon_d = 0.3$ , and (c)  $\epsilon_d = -0.3$ . Full, dashed, and dashed-dotted lines correspond to  $U = 0, 0.1, 0.3$ , respectively. The initial distributions for both the  $L$  and  $R$  reservoirs are presented by dotted lines.

### A. Anderson model with electron-electron interactions

In this section we study the evolution of the finite-size Anderson model with or without interactions, based on the three methods described earlier in Sec. III. As mentioned above, these

techniques provide the dynamics of the total DM. While the fingerprints of many-body effects are disguised in the time evolution of conventional quantities, e.g., in the dot occupation and the charge current, they are well manifested in the reservoirs' population dynamics, allowing us to discern microscopic many-body scattering processes from single-particle events.

The population  $p(\epsilon_k) = \langle c_k^\dagger c_k \rangle$  of both reservoirs, in the *noninteracting* case, is displayed in Fig. 3 at different times. We note that results obtained using the QLE framework of Sec. III A perfectly agree with numerically-exact fermionic trace formula simulations. The three panels present results using different values for the dot energy. (a) When the dot energy is placed within the bias-window ( $\epsilon_d = 0$ ) a resonance feature develops around the position of the dot level, with a dip (peak) showing in the  $L$  ( $R$ ) bath. In contrast, if the dot energy is positioned either above the bias window (b) or below it (c), a dot-assisted tunneling feature develops, with population transfer taking place around available states that are the nearest in energy to  $\epsilon_d$ . The dynamics shown in Fig. 3 is reversible, with a characteristic time  $\tau_d \sim 2\pi/\Delta E$ ,  $\Delta E = 2D/N$  is the mean spacing between energy levels and  $N = N_{L,R}$  is the number of states in the  $L, R$  baths [36]. At this characteristic time the dot population begins to vary from its QSS value due to finite size effects. This behavior can be captured with trace formula simulations, but not within the QLE approach.

In Fig. 4 we display the dynamics under a mean-field QLE treatment with parameters corresponding to Fig. 3. While we are mindful of the technique's known pathologies [38], we stress that this calculation provides an intuitive understanding of the role of interactions: Within MF, the effect of finite  $U$  is to shift features in concert with the renormalized dot energy,  $\tilde{\epsilon}_d(t) = \epsilon_d + U \langle n_d(t) \rangle$  [Eq. (26)]. Interestingly, panel (c) demonstrates a change in transport mechanism, from a dot-assisted tunneling at small  $U$ , to resonance transmission at large  $U$ , since the renormalized dot energy enters the bias window at a large enough interaction strength. Therefore, e-e interactions can enhance or suppress electronic transport, depending on the dot bare energy position.

Mean-field results are compared to numerically-exact INFPI simulations in Fig. 5 for  $U = 0.1$  and  $U = 0.3$ , with the bare dot energy centered within the bias window. Data was produced by time evolution of all  $\langle c_k^\dagger c_k \rangle$ ,  $k = l, r$ , expectation values up to  $\Gamma t \sim 4$ . In agreement with MF QLE results, the basic effect of e-e interactions observed here is a shift in the resonance position. Overall, we conclude that MF simulations can reproduce the dynamics for this set of parameters, up to  $U/\Gamma \lesssim 2$ . Qualitative features are correct through  $U/\Gamma \sim 6$ .

Convergence of INFPI is verified with respect to the time step adopted,  $\delta t$ , and the memory time accounted for,  $\tau_c$ . Representative convergence curves for  $p(\epsilon_l = \epsilon_d)$  are depicted in Fig. 6. While the time-step used does not affect our results, we note that the data is not yet fully

converged with respect to  $\tau_c$ . This slow convergence could be attributed to the long decorrelation time experienced by an electron residing on any particular bath level, since its decorrelation process should take place by following a two-step procedure: the electron should first leave the particular bath state and populate the quantum dot. From the dot, it may subsequently transfer to any other bath state. One should also note that we display here a convergence curve for a particular level. It is more accurate, but computationally demanding, to look at the overall evolution of  $p(\epsilon)$  (for all  $\epsilon$ ) with  $\tau_c$ . This is because the resonant feature may change its magnitude with  $\tau_c$ , as we see here, as well as its absolute position. Fig. 6 only analyzes the effect of  $\tau_c$  on the peak magnitude.

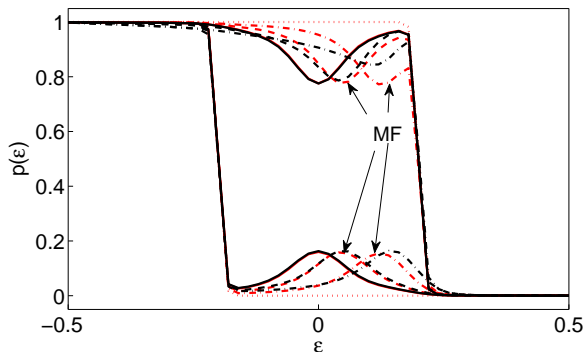


FIG. 5: Simulations of reservoirs' levels population in the resonance case,  $\epsilon_d = 0$ , at  $\Gamma t = 4$ , using INFPI (dark curves) and MF QLE (light curves). Full, dashed and dashed-dotted lines were obtained using  $U = 0, 0.1, 0.3$ , respectively. Top lines correspond to the  $L$  bath distribution, the bottom lines to the  $R$  bath. The initial distributions of both  $L$  and  $R$  reservoirs are presented by dotted lines. Parameters are the same as in Fig. 3, with  $N_{L,R} = 101$  bath states. INFPI numerical parameters are  $\delta t = 1$  and  $N_s = 7$ .

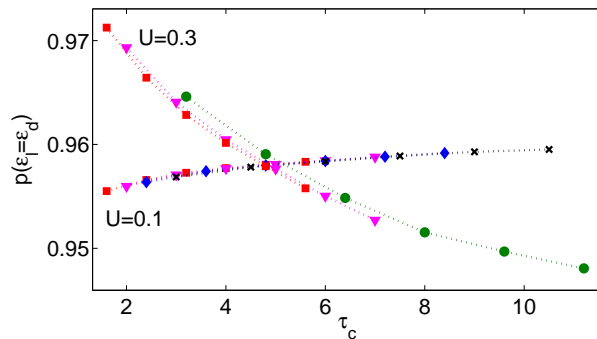


FIG. 6: Convergence trend for the INFPI data of Fig. 5. We plot  $p(\epsilon_l = \epsilon_d)$  as a function of  $\tau_c$  at  $\Gamma t = 1.2$  for  $U = 0.1$  and  $U = 0.3$ . Results are shown using different time steps,  $\delta t = 0.8$  ( $\square$ ),  $\delta t = 1.0$  ( $\nabla$ ),  $\delta t = 1.2$  ( $\diamond$ ),  $\delta t = 1.5$  ( $\times$ ) and  $\delta t = 1.6$  ( $\circ$ ). Other parameters are the same as in Fig. 5.

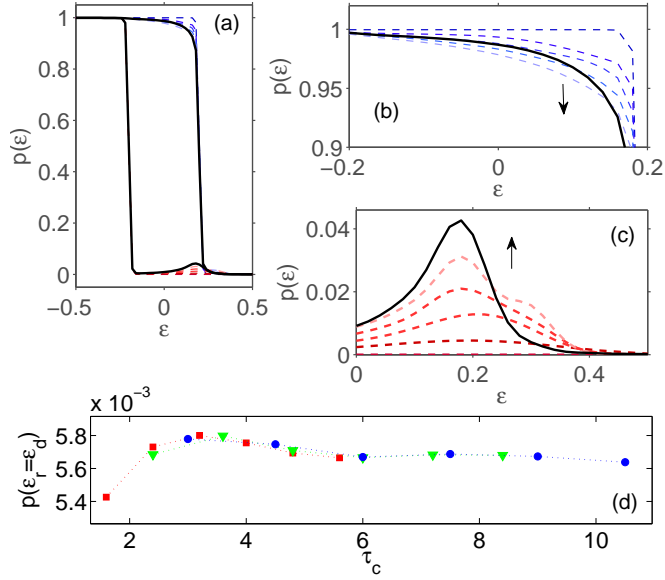


FIG. 7: (a) INFP data for the reservoirs population at different times for  $\epsilon_d = 0.25$  and  $U = 0.1$ . The five top (bottom) lines depict the population of the  $L$  ( $R$ ) baths at times  $\Gamma t = 0.05, 1, 2, 3$ , and  $4$ . (b) Zooming over the  $L$  bath population. (c) Zooming over the  $R$  bath population. The arrows indicate on the direction of time evolution. In (a)-(c) the full lines represent MF QLE data at the latest time,  $\Gamma t = 4$ . (d) Convergence behavior of  $p(\epsilon_r = \epsilon_d)$  at  $\Gamma t = 1.2$  using different time steps,  $\delta t = 0.8$  ( $\square$ ),  $\delta t = 1$  ( $\nabla$ ) and  $\delta t = 1.5$  ( $\circ$ ). Other parameters are the same as in Fig. 3, with  $N_{L,R} = 101$  bath states.

In Fig. 7 we study the dynamics of the reservoirs' levels population when the renormalized dot energy sits above the bias window,  $\tilde{\epsilon}_d > \mu_L$ . The bare energy is taken at  $\epsilon_d = 0.25$  and the interaction strength is  $U = 0.1$ . By separately calculating the time evolution of the dot occupation, to produce  $\langle n_{d,\sigma} \rangle \sim 0.12$  in the QSS limit (valid for  $\Gamma t \gtrsim 2$ ), we estimate the renormalized dot energy to be about  $\tilde{\epsilon}_d \sim 0.26$ . Overall, occupations change very slightly in time, since the dot is off-resonant thus the transport follows a dot-assisted tunneling mechanism. The reservoirs' dynamics still clearly manifests many-body effects that are not included in a MF (effective single-body) description. Essentially, we find that electrons populate high energy levels in the  $L$  and  $R$  baths up to  $\epsilon_k \sim 0.45$ . This high-energy population cannot be explained by the dot-level shift or the dot finite broadening  $\Gamma$ , as this could account for population up to  $\epsilon_k \sim 0.35$  only, see MF data (full line) in panel (c). It should be noted that the population of levels that are initially empty,  $p(\epsilon > \mu_L)$ , develops identically at the  $L$  and  $R$  reservoirs. In other words, the high energy tails in panel (c) represent the occupation of states both in the  $L$  and  $R$  baths. Supporting convergence behavior is included in panel (d). We have also performed simulations when taking a stronger interaction,  $U = 0.3$  and  $\epsilon_d = 0.15$ , to yield  $\tilde{\epsilon} \sim 0.21$ . In this case the population shows a high-

energy tail that is further enhanced with respect to MF data, representing significant deviations from a single particle description. However, as we did not manage to fully converge these results, they are not included here.

The breakdown of the single-particle picture is difficult to discern in cumulative quantities such as the charge current and the dot occupation, the latter is presented in Fig. 8, where we follow the time evolution of this quantity using four different techniques: MF QLE equations, first-order perturbation theory method [34], Monte-Carlo simulations [41–44] and INFPI [15]. The comparison shows a very good agreement between the latter two exact methods up to  $\Gamma t \sim 1$  [15]. MF QLE theory and first-order perturbation expansion both predict the correct behavior at  $U/\Gamma \lesssim 2$ . At strong interactions ( $U/\Gamma \sim 6$ ), perturbation theory fails, while MF QLE equations still provides correct qualitative behavior for  $\langle n_{d,\sigma} \rangle$ . Note that we implement a sharp cutoff at  $D = \pm 1$  in all methods. Since we do not account for the (small) energy shift in Eq. (17), MF QLE data suffer from a small shift in values, see also Fig. 2.

Naively considering the dot occupation only, one may conclude that at  $U/\Gamma \lesssim 6$  many-body effects are contained in a mean-field, effective single-body, description. However, traces of energy resolved reservoirs' dynamics as we show in Fig. 7 expose the existence of interaction effects beyond mean-field, resulting in levels population beyond the resonance width. The dot occupation thus *withholds* mechanisms involved in the transport process, while detailed reservoirs' level population can illuminate extant many-body effects and their energy resolution.

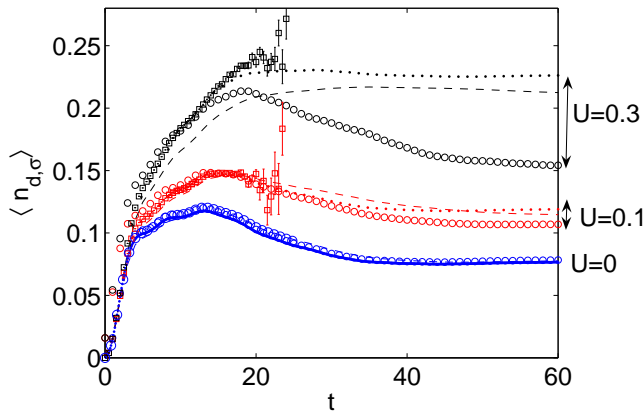


FIG. 8: Dot occupation as a function of time, generated from four different methods: INFPI (dotted), Monte-Carlo simulations ( $\square$ ) [41–44], MF QLE equations (dashed) and perturbation theory treatment ( $\circ$ ) [34]. Results are shown for three setups, bottom to top:  $\epsilon_d = 0.3$  with  $U = 0$ ,  $\epsilon_d = 0.25$  with  $U = 0.1$ , and  $\epsilon_d = 0.15$  with  $U = 0.3$ . Other parameters are the same as in Fig. 3, with  $\delta t = 1$ ,  $N_s = 7$  and  $N_{L,R} = 101$  bath states.

We now comment on the simulation time of a convergence analysis as presented in Fig. 6, covering three different time steps and  $N_s = 2, \dots, 7$ . Convergence should in principle be verified for all bath states ( $N_L + N_R = 101 \times 2$ ) and at all times. In practice, we have tested it for representative states only. The MATLAB implementation of the computational algorithm took advantage of the MATLAB built-in multi-threaded parallel features and utilized 100% of all available CPU cores on a node. When executed on one cluster node with two quad-core 2.2GHz AMD Opteron cpus and 16GB memory, convergence analysis for each expectation value took about 7x24 hours and 250MB of memory. Computations performed on the GPC supercomputer at the SciNet HPC Consortium [45] were three times faster. Computational time scales linearly with the simulated time  $t$ . For a fixed  $N_s$  value, the computational effort does not depend on the system temperature and the value of  $U$  employed.

## B. Quantum equilibration and thermalization

The techniques developed in Sec. III provide the time evolution of the total DM of a large system, allowing us to address next the problem of equilibration and thermalization in quantum mechanics. The basic question of interest here is how do quantum systems equilibrate from a nonequilibrium initial preparation, if at all. Furthermore, it is of importance to understand under what conditions a system may approach one of the canonical ensembles of statistical mechanics.

Before addressing the equilibration problem in detail we present in Fig. 9 a more standard quantity, the steady-state dot occupation. This will serve us for motivating the study of the total DM for resolving transport mechanisms. The dot occupation is displayed here as a function of  $\Gamma_G$ , the dot-probe hybridization strength, and we show results using either a voltage probe or a dephasing probe, for different values of the dot energy position. We find that the dot occupation is insensitive to the probe condition, an observation that can be proved analytically by studying the long time behavior of Eq. (19) under either probes, Eqs. (10) or (11). It is interesting to note the crossover behavior of the dot occupation when its energy is placed above the bias window: When  $\Gamma_G < \Gamma_{L,R}$  occupation grows linearly with  $\Gamma_G$ . However, it decays as  $\Gamma_G^{-1}$  at large values, when effective dephasing and inelastic effects are strong. This behavior is similar to the thermally assisted tunneling behavior observed when using more detailed modeling [46]. It can similarly be shown that the steady-state current in the system is identical irrespective of the probe condition. Note that we restrict ourselves to the quasi steady-state region since the  $G$  bath does not serve as a proper probe before quasi steady-state sets in.

The underlying transport mechanisms are therefore *obscured* in cumulative quantities (current, occupation) in this probe model, as well as in more explicit electron-phonon modeling [47]. Details about the involved mechanisms can be resolved by studying, e.g. the current noise, inelastic electron tunneling spectra [47], and the evolution of the reservoirs population [48], as we show below in the context of quantum equilibration and thermalization.

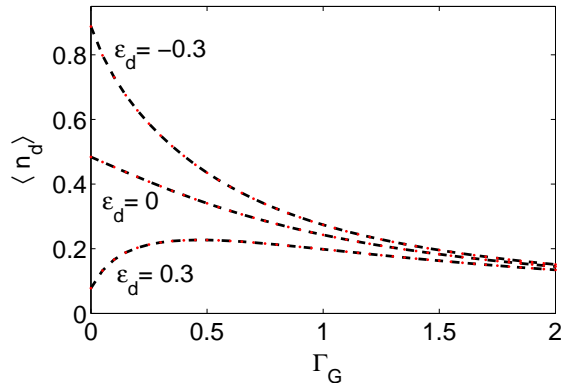


FIG. 9: Steady-state dot occupation under a voltage probe condition (dashed) and a dephasing probe (dot) for different values of the dot energy,  $\epsilon_d = -0.3, 0$  and  $0.3$ , top to bottom. Data was obtained by simulating Eq. (19) in the long time limit using  $\mu_L = -\mu_R = 0.2$ ,  $\beta = 200$  and  $\Gamma_{L,R} = 0.025$ .

The equilibration problem in quantum mechanics could be considered within different setups: a closed system [49–51], a system-bath scenario [52, 53], or taking peer quantum systems [25]. Here, we consider the Anderson model with a probe, excluding e-e interactions, and simulate the following setup: At time  $t = t_0$  we put into contact through a quantum dot two reservoirs each separately prepared in grand canonical states at chemical potentials  $\mu_\nu$  and temperature  $\beta^{-1}$ . Electrons on the dot are susceptible to either elastic-decohering processes or inelastic effects, mimicked by coupling to the relevant probe. For a schematic representation, see Fig. 1(b). Given this scenario, we investigate whether the two reservoirs can equilibrate or even thermalize in time, and furthermore, the nature of the equilibrium state. As we show below, when only elastic dephasing effects are mimicked, the system approaches a non-canonical equilibrium state. When inelastic processes are emulated, the two reservoirs relax towards a common canonical state. It should be noted that these results can be obtained for a *finite and closed* system, under a unitary evolution [23].

We identify thermal equilibration in our peer quantum system setup, by adjusting the conditions of Refs. [52, 54], demanding that: (i) The system should equilibrate, i.e., evolve towards some particular state, and stay close to it for almost all time. Furthermore, the equilibrium state should be (ii) independent of the dot properties-energetics and initial state, (iii) insensitive to the precise

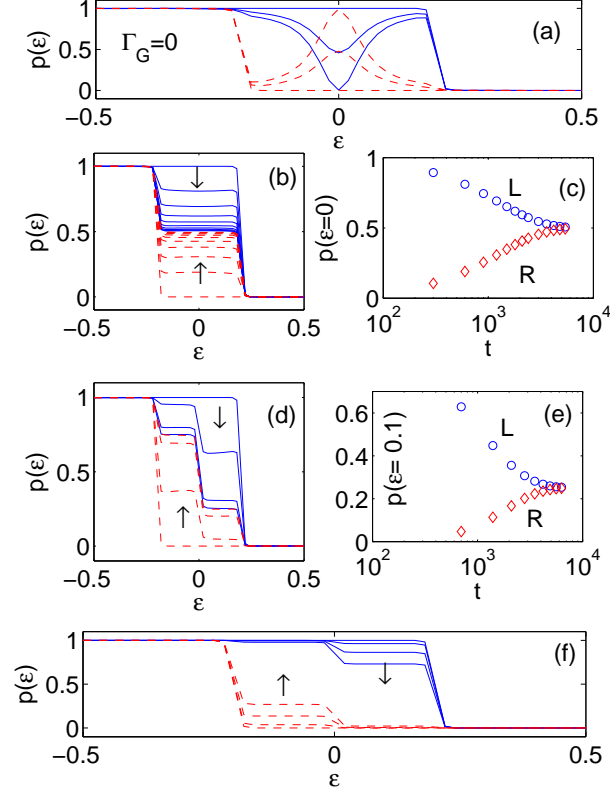


FIG. 10: Dynamics of the reservoirs population in the Anderson probe model. (a) Population of the  $L$  (full) and  $R$  (dashed) reservoirs,  $\Gamma_G = 0$ . We show results at  $t = 0, 180, 340$  as the resonance pattern develops in time. (b)-(c) Equilibration with a dephasing probe,  $\Gamma_G = 0.4$ , approaching a non-canonical equilibrium state. The  $L$  (full) and  $R$  (dashed) population are shown at  $t = 0, \delta t, \dots, 9\delta t$ ,  $\delta t = 600$ . Panel (c) demonstrates a slow-down in dynamics in approaching the equilibrium state. (d)-(f) Approaching thermal equilibrium with a voltage probe. In panel (d)  $\Gamma_G = 0.4$  with the  $L$  (full) and  $R$  dashed line population shown at  $t = 0, 700, 2800, 6300$ . Panel (e) displays the population as a function of time at a certain energy,  $\epsilon = 0.1$ . Panel (f) presents information as in (d), with  $\Gamma_G = 5$ . In all panels  $\beta = 200$ ,  $\Gamma_L = \Gamma_R = 0.025$ ,  $\epsilon_d = 0$ ,  $\mu_L = -\mu_R = 0.2$ ,  $D = 1$ ,  $N_{L,R} = 101$  and  $N_G = 2001$ . The arrows mark the direction of propagation in time.

initial state of each reservoir, (iv) close to diagonal in the energy basis of its eigen-Hamiltonian, and (v) a canonical state.

We use the trace formula, an exact unitary method, and follow the reservoirs' mutual equilibration process. We evolve the system using either a dephasing probe or a voltage probe, see Fig. 10, up to the time where recurrence features start to manifest, found here to scale as  $\tau_{rec} \propto \sum_{i=L,R,G} N_i$ . As a reference, panel (a) displays results for the model without a probe, showing the development of a resonance feature around the dot energy position at  $\epsilon_d = 0$ . A clear evolution towards an



equilibrium state is demonstrated when a probe is presented. With a dephasing probe, (b)-(c), the population of the two reservoirs relax to a two-step function with  $p(\mu_R < \epsilon < \mu_L) \sim 0.5$ . Because electrons from the  $L$  grain lose their phase memory on the dot, half populate the  $R$  side, on average, in the long time limit. This equilibrium state is sensitive to the precise details of the initial electron distribution, as energy redistribution is not allowed. We build a large  $G$  to delay recurrence behavior, but note that results at earlier times do not depend on the size of  $G$ , reinforcing the observation that  $G$  acts as an agent in driving the  $L$ - $R$  mutual equilibration. When inelastic effects are mimicked with a voltage probe, and  $\Gamma_G$  is large enough, panel (f), the system approaches a Gibbs-like thermal state—a step function at zero temperature. Results are shown up to the time  $\tau_{rec}$  at which recurrence features develop, which emerges here *before* full thermalization takes place. In order to achieve full thermalization one should further increase the size of the  $G$  bath, so as to delay recurrences. Alternatively, a dissipative mechanism could be introduced into  $G$ , e.g. by building a hierarchy of its interactions with the  $L$ - $R$  system. Using a smaller value for  $\Gamma_G$ , a non-canonical equilibrium distribution develops (d)-(e), reflecting the contribution of coherent and (effectively) incoherent electrons in the dynamics. It is also interesting to compare panels (c) and (e), displaying the equilibration progress for a dephasing probe and a voltage probe, respectively, while maintaining the value of  $\Gamma_G$ . We find that the characteristic timescale to reach equilibrium is very similar in both cases. Thus, while the probe type dictates the structure of the equilibrium state, it does not affect the equilibration timescale.

Fig. 11 shows that while under coherent evolution the resonance peak emerges around the energy  $\epsilon_d$ , in the presence of a voltage probe with (large enough)  $\Gamma_G$ , the buildup of the equilibrium state systematically occurs around the equilibrium Fermi energy. This holds even when the dot is placed *outside* the bias window (not shown). Analogous trends take place when allowing for dephasing only.

A thermal equilibrium state should be diagonal in the energy eigenbasis of its Hamiltonian [52]. In Fig. 12 we display the density matrix  $\rho_{k,k'} = \langle c_k^\dagger c_{k'} \rangle$ ,  $k, k' = l, r$ , excluding diagonal elements  $\rho_{k,k}$ , without a voltage probe (a)-(b), and with a one (c)-(d), using the QLE technique. This quantity is expected to oscillate in the long time limit since the Hamiltonian is not diagonal in the (local)  $l$  and  $r$  bases. We still show the results in the local reservoirs' basis, so as to manifest local  $\nu$ -bath properties. There are three significant differences in the behavior of off-diagonal elements, with and without the probe: (i) The absolute value of the coherences, at a given time, is smaller when  $\Gamma_G \neq 0$ . (ii) The DM approaches a diagonal form (strict diagonal values are not shown). (iii) When  $\Gamma_G = 0$ , oscillations occur around the dot energy position  $\epsilon_d$ . With the probe, contributions

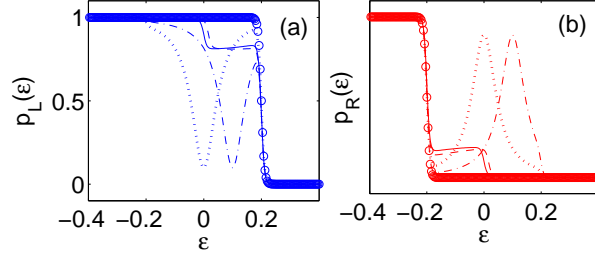


FIG. 11: (a) Occupation of  $L$  bath at time  $t = 0$  ( $\circ$ ) and  $t = 1500$  for  $\Gamma_G = 0$  and  $\epsilon_d = 0$  (dotted),  $\Gamma_G = 0$  and  $\epsilon_d = 0.1$  (dashed-dotted),  $\Gamma_G = 0.4$  and  $\epsilon_d = 0$  (full),  $\Gamma_G = 0.4$  and  $\epsilon_d = 0.1$  (dashed). The latter two lines assume the voltage probe condition. (b) Same for the  $R$  side occupations. Other parameters are the same as in Fig. 10.

are scattered, yet they appear more prominently around the equilibrium Fermi energy,  $\epsilon = 0$ . These three features should become more pronounced at longer times, which can be simulated using the trace formula approach.

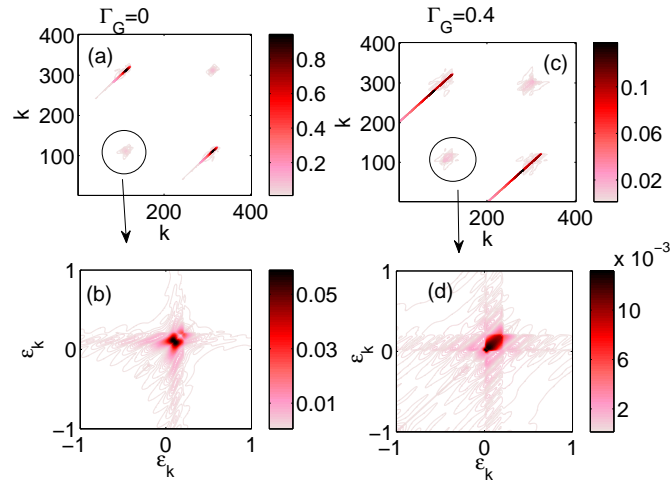


FIG. 12: Absolute values of the density matrix elements  $\rho_{k,k'}$ ,  $k, k' = l, r$ , at  $t = 600$ , excluding diagonal elements. In panel (a) and (b)  $\Gamma_G = 0$ . In panels (c) and (d) we use a voltage probe with  $\Gamma_G = 0.4$ . Panels (a) and (c) display the total density matrix, and the axes are the energy indices  $1, \dots, 402$ . The  $L$  reservoir includes the first 201 states. The rest are  $R$  bath states. Panels (b) and (d) zoom on the  $\rho_{l,l'}$  density matrix, the bottom-leftmost part of the total DM. Other parameters are  $\epsilon_d = 0.1$ ,  $\Gamma_{L,R} = 0.025$ ,  $\beta = 200$ ,  $\mu_L = -\mu_R = 0.2$ .

## V. CONCLUSION

We have extended analytical and numerical methods, developed for simulating the dynamics of impurities, i.e., subsystems attached to large reservoirs, to reveal the dynamics of the total system. As an example, we have focused on the Anderson model, a quantum dot coupled to two metal grains, and obtained the evolution of the total density matrix, focusing on the reservoirs' evolution from an initial nonequilibrium state. We have studied the noninteracting model, as well as a model with interactions and a probe model, emulating elastic dephasing and dissipation effects. The three methods presented are the analytic quantum Langevin equation approach, a simulation based on a trace formula, and an exact numerical path integral scheme that can accommodate e-e repulsion effects. Notably, the extension of the QLE treatment to provide the total DM is of general importance as it can be used in multitude of other systems, as long as one can identify a “subsystem” within the total system.

Making use of the methods developed, we have investigated the total system dynamics in the presence of distinct effects: (i) e-e interactions on the impurity, and (ii) dephasing and inelastic scattering effects. Addressing the prior, our calculations allow us to *energy resolve* the effect of e-e interactions on electron transfer in the Anderson dot model. In the resonant regime we found that the dynamics observed for noninteracting electrons is largely preserved up to  $U/\Gamma \lesssim 2$ , and the main effect of interactions on the reservoirs' occupation is apparently a simple shift in the position of features affected by the renormalization of the dot energy. Away from resonance, in the tunneling domain, the presence of weak interactions already manifested itself in scattering electrons to high energy levels, an effect that is not captured within a mean-field treatment. In the case of the later effect, we found numerically that the presence of dephasing and inelastic effects on a weak link only can lead to *global* system equilibration and even thermalization. It is important to note that no restrictions were enforced on the metals' band structure and the dot energy. This is significant in light of many other studies in which equilibration requires the “nondegenerate energy gap” condition to be satisfied [25, 49, 52].

Future directions include the study of finite temperature and electron-electron interaction effects in the equilibration process [15], and the behavior given a quantum dot chain between the two metal grains. In a linear chain of impurities we expect that the coherent-diffusive crossover in the charge current behavior [55] would similarly manifest itself in the energy reorganization process of the reservoirs. The methods developed here could also be adopted for the study of bosonic systems, e.g., to describe the dynamics of bosonic degrees of freedom interacting with harmonic baths.

## Acknowledgments

This work has been supported by an NSERC discovery grant. M.K. thanks Diptiman Sen for useful discussions. The authors acknowledge T. L. Schmidt for providing the time-dependent perturbation theory code. The work of K.L.T. has been supported by an Early Research Award of D.S. Computations were performed on the GPC supercomputer at the SciNet HPC Consortium [45]. SciNet is funded by: the Canada Foundation for Innovation under the auspices of Compute Canada; the Government of Ontario; Ontario Research Fund - Research Excellence; and the University of Toronto.

## Appendix A: Density matrix elements in the quantum Langevin approach

We provide here the explicit expressions for the density matrix elements  $\rho_{l,k}$ ,  $k \in L, R$ . The population is calculated by evaluating the correlation functions in Eq. (24), using Eqs. (13) and (18), to yield

$$p(\epsilon_l) = \langle c_l^\dagger(t_0)c_l(t_0) \rangle + F_2 + F_3 \quad (\text{A1})$$

The first term accommodates the initial condition. The second ( $F_2$ ) and the third ( $F_3$ ) terms are given by

$$\begin{aligned} F_2 &= -v_l^2 f_l \frac{2\Gamma}{\Gamma^2 + \epsilon_{dl}^2} t - 2v_l^2 f_l \frac{\epsilon_{dl}^2 - \Gamma^2}{(\epsilon_{dl}^2 + \Gamma^2)^2} + \frac{v_l^2 f_l e^{-\Gamma t}}{(\epsilon_{dl}^2 + \Gamma^2)^2} \left\{ 2(\epsilon_{dl}^2 - \Gamma^2) \cos(\epsilon_{dl} t) + 4\epsilon_{dl} \Gamma \sin(\epsilon_{dl} t) \right\} \\ F_3 &= v_l^2 \sum_{k=l,r} \frac{v_k^2 f_k}{\Gamma^2 + \epsilon_{dk}^2} \left\{ \frac{4 \sin^2\left(\frac{\epsilon_{lk} t}{2}\right)}{\epsilon_{lk}^2} + \frac{1}{\Gamma^2 + \epsilon_{dl}^2} \left[ e^{-2\Gamma t} + 1 - e^{t(i\epsilon_{dl} - \Gamma)} - e^{-t(i\epsilon_{dl} + \Gamma)} \right] \right. \\ &\quad \left. + \left[ \frac{1 - e^{-t(\Gamma + i\epsilon_{dl})} + e^{-t(\Gamma + i\epsilon_{dk})} - e^{-it\epsilon_{lk}}}{(\epsilon_{dl} - i\Gamma) \epsilon_{lk}} + c.c. \right] \right\}. \end{aligned} \quad (\text{A2})$$

Inter and intra-reservoir coherences, e.g.  $\rho_{l,k}(t)$ ,  $k \in L, R$  can be similarly calculated. Here, one should distinguish between the cases  $\epsilon_l = \epsilon_k$  and  $\epsilon_l \neq \epsilon_k$ . In the latter case we find that

$$\rho_{l,k}(t) \equiv \langle c_l^\dagger(t)c_k(t) \rangle = A_1 + A_2 + A_3 \quad (\text{A3})$$

where

$$\begin{aligned} A_1 &= -\frac{v_k v_l f_l}{\Gamma + i\epsilon_{dl}} \left[ \frac{e^{-t(\Gamma + i\epsilon_{dl})} - e^{i\epsilon_{lk} t}}{\Gamma + i\epsilon_{dk}} + \frac{i}{\epsilon_{lk}} (1 - e^{i\epsilon_{lk} t}) \right] \\ A_2 &= -\frac{v_l v_k f_k}{\Gamma - i\epsilon_{dk}} \left[ \frac{e^{-t(\Gamma - i\epsilon_{dk})} - e^{i\epsilon_{lk} t}}{\Gamma - i\epsilon_{dl}} + \frac{i}{\epsilon_{lk}} (1 - e^{i\epsilon_{lk} t}) \right] \end{aligned}$$

and

$$\begin{aligned}
A_3 = & v_l v_k \sum_{k' \in L, R} \frac{v_{k'}^2 f_{k'}}{\Gamma^2 + \epsilon_{dk'}^2} \\
& \times \left\{ \frac{1}{\epsilon_{k'l} \epsilon_{k'k}} + \frac{e^{it\epsilon_{lk'}}}{\epsilon_{lk'} \epsilon_{k'k}} - \frac{e^{it\epsilon_{lk}}}{\epsilon_{lk'} \epsilon_{k'k}} - \frac{e^{it\epsilon_{k'k}}}{\epsilon_{k'l} \epsilon_{k'k}} + \frac{e^{it\epsilon_{k'k}} + e^{-t(\Gamma+i\epsilon_{dl})} - e^{it\epsilon_{lk}} - e^{-t(\Gamma+i\epsilon_{dk'})}}{\epsilon_{lk'}(i\Gamma + \epsilon_{kd})} \right. \\
& \left. + \frac{e^{it\epsilon_{lk'}} + e^{-t(\Gamma-i\epsilon_{dk})} - e^{it\epsilon_{lk}} - e^{-t(\Gamma-i\epsilon_{dk'})}}{\epsilon_{k'k}(i\Gamma + \epsilon_{dl})} + \frac{e^{-2\Gamma t} + e^{it\epsilon_{lk}} - e^{-t(\Gamma+i\epsilon_{dl})} - e^{-t(\Gamma-i\epsilon_{dk})}}{(i\Gamma + \epsilon_{dl})(-i\Gamma + \epsilon_{dk})} \right\}.
\end{aligned}$$

In the resonant limit,  $\epsilon_l = \epsilon_k$  and  $k \notin L$ , a simpler result is obtained,

$$\langle c_l^\dagger(t) c_k(t) \rangle = A_1^r + A_2^r + A_3^r \tag{A4}$$

with

$$\begin{aligned}
A_1^r &= -\frac{v_k v_l f_l}{\Gamma + i\epsilon_{dl}} \left[ t - \frac{1 - e^{-t(\Gamma+i\epsilon_{dl})}}{\Gamma + i\epsilon_{dl}} \right] \\
A_2^r &= -\frac{v_l v_k f_k}{\Gamma - i\epsilon_{dl}} \left[ t - \frac{1 - e^{-t(\Gamma-i\epsilon_{dl})}}{\Gamma - i\epsilon_{dl}} \right] \\
A_3^r &= \frac{v_k}{v_l} F_3.
\end{aligned}$$

- 
- [1] Polkovnikov A, Sengupta K, Silva A and Vengalattore M 2011 *Rev. Mod. Phys.* **83** 863
  - [2] Bloch I, Dalibard J and Zwerger W 2008 *Rev. Mod. Phys.* **80** 885
  - [3] Houck A A, Tureci H E and Koch J 2012 *Nature Phys.* **8** 292
  - [4] Anderson P W 1961 *Phys. Rev.* **124** 41
  - [5] Konik R M, Saleur H and Ludwig A W W 2001 *Phys. Rev. Lett.* **87** 236801
  - [6] Anders F B and Schiller A 2005 *Phys. Rev. Lett.* **95** 196801
  - [7] Schiro M and Fabrizio M 2009 *Phys. Rev. B* **79** 153302
  - [8] Weiss S, Eckel J, Thorwart M and Egger R 2008 *Phys. Rev. B* **77** 195316
  - [9] Eckel J, Heidrich-Meisner F, Jakobs S G, Thorwart M, Pletyukhov M and Egger R 2010 *New J. Phys.* **12** 043042
  - [10] Ford G W, Lewis J T and OConnell R F 1988 *Phys. Rev. A* **37** 4419
  - [11] Dhar A and Sen D 2006 *Phys. Rev. B* **73** 085119
  - [12] Dhar A, Saito K and Hanggi P 2012 *Phys. Rev. E* **85** 011126
  - [13] Klich I 2003 *Quantum Noise in Mesoscopic Systems* (Kluwer)
  - [14] Segal D, Millis A J and Reichman D R 2011 *Phys. Chem. Chem. Phys.* **13** 14378
  - [15] Segal D, Millis A J and Reichman D R 2010 *Phys. Rev. B* **82** 205323

- [16] Muhlbacher L and Rabani E 2008 *Phys. Rev. Lett.* **100** 176403
- [17] Wang H, Pshenichnyuk I, Hartle R and Thoss M 2011 *J. Chem. Phys.* **135** 244506
- [18] Hutzen R, Weiss S, Thorwart M and Egger R 2012 *Phys. Rev. B* **85** 121408
- [19] Vinkler Y, Schiller A and Andrei N 2012 *Phys. Rev. B* **85** 035411
- [20] Buttiker M 1985 *Phys. Rev. B* **32** 1846
- [21] Buttiker M 1986 *Phys. Rev. B* **33** 3020
- [22] de Jong M J M and Beenakker C W J 1996 *Physica A* **230** 219
- [23] Kulkarni M, Tiwari K L and Segal D 2012 *arXiv:1206.2408*
- [24] Ponomarev A V, Denisov S, Hanggi P and Gemmer J 2012 *Eur. Phys. Lett.* **98** 40011
- [25] Ponomarev A V, Denisov S and Hanggi P 2011 *Phys. Rev. Lett.* **106** 010405
- [26] Ajisaka S, Barra F, Mejia-Monasterio C and Prosen T 2012 *arXiv:1204.1321*
- [27] Buttiker M 1988 *Phys. Rev. B* **38** 9375
- [28] Forster H, Samuelsson P, Pilgram S and Buttiker M 2007 *Phys. Rev. B* **75** 035340
- [29] Nigg S E and Buttiker M 2008 *Phys. Rev. B* **77** 085312
- [30] Roulleau P, Portier F, Roche P, Cavanna A, Faini G, Gennser U and Mailly D 2009 *Phys. Rev. Lett.* **102** 236802
- [31] Roy D and Dhar A 2007 *Phys. Rev. B* **75** 195110
- [32] Press W H, Flannery B P, Teukosky S A and Vetterling W T 1992 *Numerical Recipes in C: The Art of Scientific Computing* (Cambridge University Press)
- [33] Eq. (9) can be justified by repeating the steps leading to Eq. (23), and taking the long-time limit
- [34] Schmidt T L, Werner P, Muhlbacher L and Komnik A 2008 *Phys. Rev. B* **78** 235110
- [35] For dense reservoirs, one could replace the summation by an integral over frequency. However, since we are simulating the dynamics using finite number of bath states, we prefer to show our results in its discrete form
- [36] Yukalov V I 2011 *Laser Phys. Lett.* **8** 485
- [37] Komnik A and Gogolin A O 2004 *Phys. Rev. B* **69** 153102
- [38] Horvath B, Lazarovits B, Sauret O and Zarand G 2008 *Phys. Rev. B* **77** 113108
- [39] Bedkhal S and Segal D 2012 *Phys. Rev. B* **85** 155324
- [40] Hirsch J E 1983 *Phys. Rev. B* **28** 4059
- [41] Werner P, Comanac A, de Medici L, Troyer M and Millis A J 2006 *Phys. Rev. Lett.* **97** 076405
- [42] Gull E, Werner P, Millis A and Troyer M 2007 *Phys. Rev. B* **76** 235123
- [43] Werner P, Oka T and Millis A J 2009 *Phys. Rev. B* **79** 035320
- [44] Werner P, Oka T, Eckstein M and Millis A J 2010 *Phys. Rev. B* **81** 035108
- [45] Loken C and et al 2010 *J. Phys.: Conf. Ser.* **256** 012026
- [46] Segal D, Nitzan A, Davis W B, Wasielewsky M R and Ratner M A 2000 *J. Phys. Chem.* **104** 3817
- [47] Galperin M, Ratner M A and Nitzan A 2007 *J. Phys.: Condens. Matter* **19** 103201
- [48] Segal D and Nitzan A 2002 *Chem. Phys.* **281** 235

- [49] Reimann P 2010 *New J. Phys.* **12** 055027
- [50] Reimann P 2008 *Phys. Rev. Lett.* **101** 190403
- [51] Short A J 2011 *New J. Phys.* **13** 053009
- [52] Linden N, Popescu S, Short A J and Winter A 2009 *Phys. Rev. E* **79** 061103
- [53] Dajka J, Luczka J and Hanggi P 2011 *Phys. Rev. A* **84** 032120
- [54] Gogolin C, Muller M P and Eisert J 2011 *Phys. Rev. Lett.* **106** 040401
- [55] Bonetto F, Lebowitz J L and Lukkarinen J 2004 *J. Stat. Phys.* **116** 783